HELDA
HELSINGIN YLIOPISTO
HELSINGFORS UNIVERSITET
UNIVERSITY OF HELSINKI

UNIVERSITY OF HELSINKI

https://helda.helsinki.fi

# Anatomical atlas of the upper part of the human head for electroencephalography and bioimpedance applications

Moura, Fernando S.

2021-11-26

Moura , F S , Beraldo , R G , Ferreira , L A & Siltanen , S 2021 , ' Anatomical atlas of the upper part of the human head for electroencephalography and bioimpedance applications ' , Physiological Measurement , vol. 42 , no. 10 , 105015 . https://doi.org/10.1088/1361-6579/ac3218

http://hdl.handle.net/10138/337492
https://doi.org/10.1088/1361-6579/ac3218

cc_by
publishedVersion

*Downloaded from Helda, University of Helsinki institutional repository.*

*This is an electronic reprint of the original article.*

*This reprint may differ from the original in pagination and typographic detail.*

*Please cite the original version.*

Physiological Measurement

IPEM
Institute of Physics and Engineering in Medicine

PAPER • OPEN ACCESS

# Anatomical atlas of the upper part of the human head for electroencephalography and bioimpedance applications

To cite this article: Fernando S Moura *et al* 2021 *Physiol. Meas.* **42** 105015

View the article online for updates and enhancements.

You may also like

- Spinal pedicle screw planning using deformable atlas registration
J Goerres, A Uneri, T De Silva et al.
- PatcherBot: a single-cell electrophysiology robot for adherent cells and brain slices
Ilya Kolb, Corey R Landry, Mighten C Yip et al.
- Open Ephys: an open-source, plugin-based platform for multichannel electrophysiology
Joshua H Siegle, Aarón Cuevas López, Yogi A Patel et al.

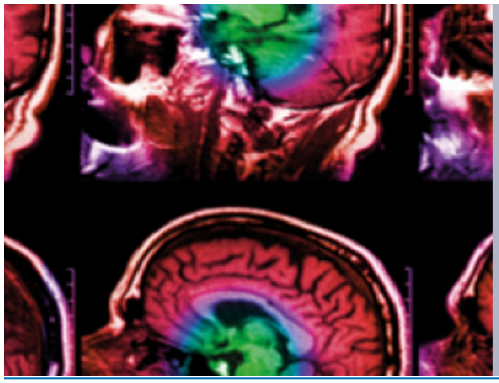

IPEM | IOP
Series in Physics and Engineering in Medicine and Biology

Your publishing choice in medical physics, biomedical engineering and related subjects.

Start exploring the collection–download the first chapter of every title for free.

This content was downloaded from IP address 128.214.163.77 on 14/12/2021 at 13:29

IOP Publishing Physiol. Meas. 42 (2021) 105015 https://doi.org/10.1088/1361-6579/ac3218

Physiological Measurement

IPEM Institute of Physics and Engineering in Medicine

OPEN ACCESS

RECEIVED
7 July 2021

REVISED
16 October 2021

ACCEPTED FOR PUBLICATION
21 October 2021

PUBLISHED
26 November 2021

Original content from this work may be used under the terms of the Creative Commons Attribution 4.0 licence.

Any further distribution of this work must maintain attribution to the author(s) and the title of the work, journal citation and DOI.

PAPER

# Anatomical atlas of the upper part of the human head for electroencephalography and bioimpedance applications

**Fernando S Moura**[1,2], **Roberto G Beraldo**[1], **Leonardo A Ferreira**[1] and **Samuli Siltanen**[2]

[1] Engineering, modelling and Applied Social Sciences Center, Federal University of ABC São Bernardo do Campo, São Paulo, Brazil
[2] Department of Mathematics and Statistics, University of Helsinki, Helsinki, Finland

**E-mail:** fernando.moura@ufabc.edu.br

**Keywords:** anatomical atlas, cerebral circulation, electrical properties, human head model, electrophysiology, electrical impedance tomography, electroencephalography

## Abstract

*Objective.* The objective of this work is to develop a 4D (3D+T) statistical anatomical atlas of the electrical properties of the upper part of the human head for cerebral electrophysiology and bioimpedance applications. *Approach.* The atlas was constructed based on 3D magnetic resonance images (MRI) of 107 human individuals and comprises the electrical properties of the main internal structures and can be adjusted for specific electrical frequencies. T1w+T2w MRI images were used to segment the main structures of the head while angiography MRI was used to segment the main arteries. The proposed atlas also comprises a time-varying model of arterial brain circulation, based on the solution of the Navier–Stokes equation in the main arteries and their vascular territories. *Main results.* High-resolution, multi-frequency and time-varying anatomical atlases of resistivity, conductivity and relative permittivity were created and evaluated using a forward problem solver for EIT. The atlas was successfully used to simulate electrical impedance tomography measurements indicating the necessity of signal-to-noise between 100 and 125 dB to identify vascular changes due to the cardiac cycle, corroborating previous studies. The source code of the atlas and solver are freely available to download. *Significance.* Volume conductor problems in cerebral electrophysiology and bioimpedance do not have analytical solutions for nontrivial geometries and require a 3D model of the head and its electrical properties for solving the associated PDEs numerically. Ideally, the model should be made with patient-specific information. In clinical practice, this is not always the case and an average head model is often used. Also, the electrical properties of the tissues might not be completely known due to natural variability. Anatomical atlases are important tools for *in silico* studies on cerebral circulation and electrophysiology that require statistically consistent data, e.g. machine learning, sensitivity analyses, and as a benchmark to test inverse problem solvers.

## 1. Introduction

Electrophysiology is the branch of physiology that investigates the electrical properties of biological tissues. The analysis is based on electrical measurements, voltages, or electric currents, generated by the tissue or in response to external electric stimuli.

One special group is clinical neurophysiology, where the bioelectrical activity is recorded to assess central and peripheral nervous systems. Electroencephalography (EEG) is an important monitoring and diagnostic method in this speciality to record brain electrical activity that can be used to diagnose thalamocortical rhythms, such as assessing seizure disorders, epilepsy, sleep disorders, coma, schizophrenia, Parkinson disease, and brain death (Michel and Brunet 2019, Jatoi and Kamel 2017).

Electroencephalography measures voltage variations using multiple electrodes typically placed along the scalp of the patient. The measured voltages are the result of ionic currents inside the brain, therefore they are caused by spontaneous electrical activity.

© 2021 The Author(s). Published on behalf of Institute of Physics and Engineering in Medicine by IOP Publishing Ltd

In the case of epilepsy diagnostics, EEG is employed to determine the type, location, and extension of the lesion causing seizures. This is a challenging task since it depends on measurements taken on the surface of the scalp to infer the internal source of the disorder, a process called source reconstruction (Hallez *et al* 2007, Grech *et al* 2008).

Bioimpedance analysis is another group of methods used to assess the electrical properties of biological tissues. Measurements are made in response to external stimuli, such as measuring voltages caused by external current sources attached to the surface of the body or vice-versa.

Electrical impedance tomography (EIT) is a medical image technique in which electrical measurements on the surface of the body are used to create an image of conductivity distribution (or admittivity, the complex-valued equivalent) within the body. The image can then be associated with the physiological conditions of the patient. EIT has been used successfully in many areas, such as in lung applications to monitor acute respiratory distress syndrome, obstructive lung diseases or perioperative patients (Martins *et al* 2019), monitoring mechanical ventilation, heart activity (Frerichs *et al* 2016), cardiac function and detecting cancerous tissues (Adler and Boyle 2019). It is also being investigated to monitor brain activity and to distinguish between ischemic and hemorrhagic stroke (Adler and Boyle 2019).

Many electrophysiology applications require solving a nonlinear ill-posed inverse problem associated with the volume conductor. Reliable and stable solutions depend on prior information about the geometry and electrical properties of the tissues and knowledge about measurement uncertainty. In the case of source reconstruction, prior information about the electrical properties of the tissues is required for composing the forward volume conduction model needed in the process. Small errors in the electrical properties inside the head can obfuscate the effects of deep brain activity. In the case of EIT, anatomical and electrical prior information is also required to restrict the solution search space.

In addition, the brain is not a static structure. The flow of blood varies periodically during each cardiac cycle (Wagshul *et al* 2011). Intracranial pulsatility has been evaluated using magnetic resonance imaging (Vikner *et al* 2019, Holmgren *et al* 2019), or transcranial Doppler sonography (Kneihsl *et al* 2020), and tissue pulsatility imaging (Kucewicz *et al* 2008, Desmidt *et al* 2018).

Blood flow centre-line velocity and artery radius influence the electrical impedance of blood in that artery (Gaw *et al* 2008, Shen *et al* 2016, 2018). This makes it promising to use electrical conductivity measurements, such as in EIT or impedance cardiography, in haemodynamic monitoring using surface electrodes on the skin. In fact, there have been several works recently aiming to monitor blood flow and/or pressure waveforms using them, e.g. common carotid arteries (Zhang *et al* 2020), aortic artery (Badeli *et al* 2020), pulmonary artery (Braun *et al* 2018), radial artery (Pesti *et al* 2019), and cerebral arteries (Beraldo and Moura 2020). There are works about impedance cardiography to determine stroke volume (Bernstein 2010), electrical bioimpedance sensing to determine the central aortic pressure curves (Min *et al* 2019), and pulmonary artery pressure estimation using EIT (Proença *et al* 2020). There is an increasing interest in brain monitoring using electrical measurements, such as to monitor ventricular volume (Wembers *et al* 2019), rheoencephalography to assess cerebral blood flow (Bodo *et al* 2018, Meghdadi *et al* 2019), brain perfusion of rats (Dowrick *et al* 2016, Song *et al* 2018), and stroke identification (Goren *et al* 2018, Agnelli *et al* 2020, Candiani and Santacesaria 2020, Candiani *et al* 2019).

Volume conductor problems in electrophysiology and bioimpedance do not have analytical solutions for nontrivial geometries and rely on numerical methods, e.g. finite element method (FEM) to discretize the head in small elements and solve the associated PDEs. Ideally, the FEM model should be built with patient-specific information, taken from MRI or CT scans to capture precisely the geometry of the head, its internal structures, and electrode positions. Unfortunately, in clinical practice, this is not the case. Often, an oversimplified geometry is employed for all patients due to the lack of computational tools and time.

The effects of mismodelling have been investigated before. EEG source localization errors increase substantially when individual-specific head models are not at disposal (Acar and Makeig 2013). The authors also show that errors in the conductivity of the skull cause large estimate errors. The latter is especially challenging because the electrical properties of the skull are highly heterogeneous and have large variability inter-individual. Cerebrospinal fluid (CSF) has a big impact on the results due to its high conductivity that forms a conductive layer surrounding the brain effectively shielding the interior (Vorwerk *et al* 2014, Cho *et al* 2015). Also, the authors show that distinguishing white and grey matters also impact the head volume conductor model.

The objective of this work is to develop a statistical anatomical atlas of electrical properties of the upper part of the human head for electrophysiology and bioimpedance applications. The atlas is constructed based on MRI images of human individuals and comprises the electrical properties of the main structures for electrophysiology. The proposed atlas also comprises a time-varying model of the brain circulation, based on the solution of the Navier–Stokes equation for blood flow in the main arteries (Melis *et al* 2017, Melis 2018). The atlas can be used to generate synthetic data statistically consistent with the population to compose learning sets for machine learning methods, for sensitivity analyses, and as a benchmark to test algorithms. The atlas can also

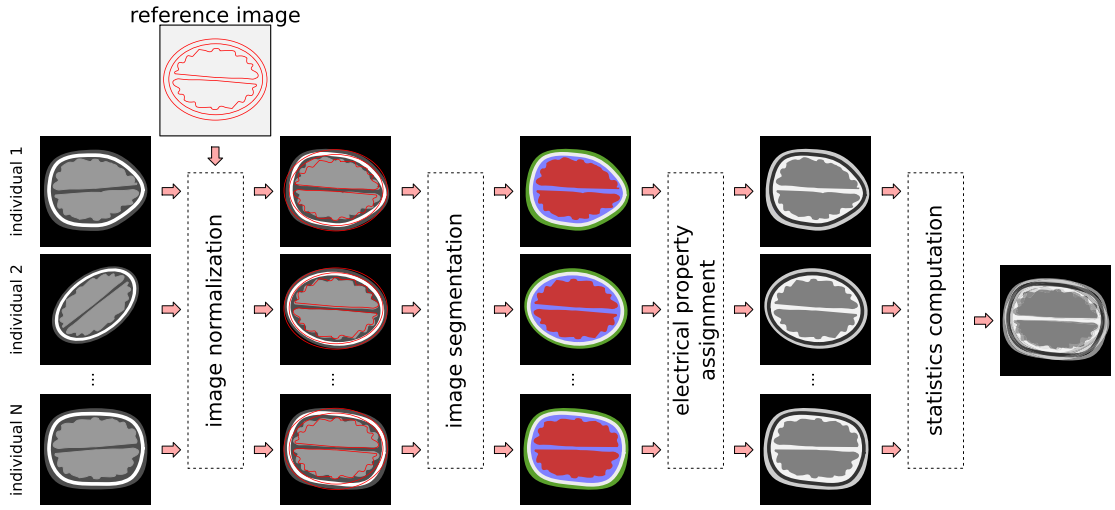


**Figure 1.** Main steps necessary to compute the static component of the anatomical atlas. Each image is normalized to a reference image, segmented into the main compartments. Each segment is assigned with the corresponding electrical property and, finally, the statistics of the atlas can be estimated.

be used as statistical prior information for inverse problems in electrophysiology. Anatomy-based priors are found in the literature, such as for thorax applications (Martins *et al* 2019, Kaipio and Somersalo 2005).

## 2. Anatomical atlas description and construction

The anatomical atlas is composed of a static component $A_s$ with the electrical properties of the main tissues found in the upper part of the human head and a dynamic component $A_d(t)$ to account for blood perfusion dynamics in the human head. The two components of the atlas are considered Gaussian and independent, therefore the final statistics of the atlas $A$ is composed by

$$A_s \sim N(\bar{x}_s, \mathbf{\Gamma}_s), \tag{1}$$

$$A_d(t) \sim N(\bar{x}_d(t), \mathbf{\Gamma}_d(t)), \tag{2}$$

$$A(t) \sim N(\bar{x}_s + \bar{x}_d(t), \mathbf{\Gamma}_s + \mathbf{\Gamma}_d(t)). \tag{3}$$

The two components of the atlas are presented in details in the following subsections.

### 2.1. Static component

The static component of the atlas distinguishes five main compartments of importance for electrophysiology of the human head: grey matter (GM), white matter (WM), cerebrospinal fluid (CSF), bones (BO) and other soft tissues (OT). Figure 1 depicts the general procedure to calculate the static component of the anatomical atlas.

3D Magnetic Resonance (MR) images of 107 healthy human individuals, made available by the CASILab at the University of North Carolina at Chapel Hill, were used to build the atlas (Bullitt *et al* 2005). The MR images were obtained in a three-tesla equipment with a resolution of $1 \times 1 \times 1$ mm. An equal number of male and female individuals were used, with an average age of $43 \pm 15$ years old. The dataset contains T1w and T2w MR images of each patient and are both used to improve skull segmentation (Nielsen *et al* 2018) as described below.

The symmetric image normalization (SyN) method was applied to the images to diminish differences due to misalignment, aspect ratio, and sizes between the heads (Avants *et al* 2008). For this purpose, the advanced normalization tools was used, under the Neuroimaging in Python Pipelines and Interfaces (Nipype) framework (Gorgolewski *et al* 2011). Detailed information regarding the normalization can be found in Avants *et al* (2008, 2009).

Each of the 214 ($2 \times 107$) images was transformed aiming to maximize its similarity with a reference image. The reference image is the MNI ICBM 152[3], a nonlinear symmetric atlas with $1 \times 1 \times 1$ mm resolution (Grabner *et al* 2006, Fonov *et al* 2009). The reference image is presented in figure 2. Using an average head geometry as reference avoids having to choose one of the images in the dataset as reference, eliminating the possibility of choosing as a reference an individual with any abnormal geometric feature. Each transformation is

[3] Available at http://nist.mni.mcgill.ca/?p=858

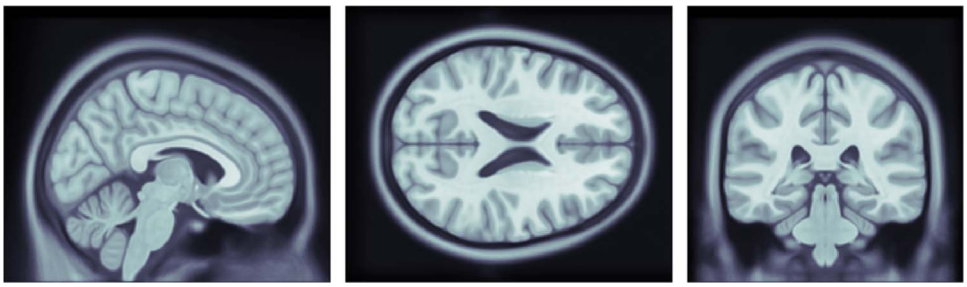

**Figure 2.** Slices of the reference image MNI ICBM 152.

performed in two stages, first a rigid transformation to roughly align the geometries, followed by an affine transformation.

The normalization process assumes the heads have similar shapes and proportions. Therefore, the atlas represents a head with size and proportions similar to the reference head used for the normalization. If necessary, the resulting atlas can be transformed to accommodate other geometries, for example when the geometry of the head of the patient is available or if an average head model is preferred. This procedure will be described in section 3.3.

After the spatial normalization, the images were segmented into six classes: background, WM, GM, CSF, BO, and OT. The statistical parametric mapping (SPM) was used to segment the images (Frackowiak *et al* 2004).

Compact bones produce very low MR signals, causing difficulties for skull segmentation. A recent study by Nielsen *et al* (2018) presents an analysis on the performance of bone segmentation using various toolboxes commonly employed to segment the human head against CT-based skull segmentation. The authors show that SPM outperforms other methods in the study when the multi-channel (T1w+T2w) strategy is employed. The inclusion of T2w increases the contrast between scalp, compact bone and CSF and greatly reduces the presence of outliers with bad segmentation, substantially reducing the variance across subjects. This combination also increases the contrast between soft tissues (Misaki *et al* 2014). The authors also describe that SPM's multi-channel segmentation (T1w+T2w) inaccuracies compared to CT segmentation manifest mainly as false positives around the air cavities and false negatives around the vertebrae. For the proposed atlas, segmentation errors between bone and air is not an issue due to their high resistivities while the vertebrae region is out of the scope of the atlas proposed in this work.

We employed SPM's multi-channel segmentation (T1w+T2w) following the guidelines from Nielsen *et al* (2018). The method is composed of a preprocessing step where T1w and T2w images are coregistered maximizing mutual information, followed by circular optimization of three components: (i) modelling of the intensities of the images using a Gaussian mixture model; (ii) normalization of tissue probability maps of the five parts of the head with the images; and (iii) a bias field correction. Further details about the implementation can be found in Ashburner and Friston (2005). At the end of this phase, each voxel of the images is assigned to the label with the highest probability.

Three additional steps were also performed to improve segmentation. (i) Any segmentation holes inside the head were filled with the nearest tissue in the image. This procedure was applied to all 2D slices in the three anatomical planes of each image, (ii) small segmentation artefacts outside the human head were removed by isolating the largest connected group in the image using a six-connected neighbourhood strategy. (iii) Four iterations of morphological opening operation to the binary mask of the head to smooth the external surface of the head.

*2.1.1. Electrical properties of the segments*

Each voxel of the segmented images was assigned to the electrical property of the corresponding tissue before computing the statistics of the atlas. Tissues were modelled as isotropic, even though it is known that some tissues are anisotropic. The electrical properties depend on the type, physiological conditions and frequency in consideration (Gabriel *et al* 1996, 1996a).

Given the angular frequency of the electrical signal $\omega = 2\pi f$, the complex relative permittivity $\hat{\epsilon}(\omega)$ of a tissue can be modelled as the sum of four Cole–Cole dispersion terms (Gabriel *et al* 1996b)

$$\hat{\epsilon}(\omega) = \epsilon_\infty + \sum_{n=1}^{4} \frac{\Delta\epsilon_n}{1 + (j\omega\tau_n)^{1-\alpha_n}} + \frac{\sigma_0}{j\omega\epsilon_0}, \tag{4}$$

where $\epsilon_0$ is the permittivity of free space and all the other parameters depend on the tissue (Gabriel *et al* 1996b, Andreuccetti *et al* 1997). The conductivity $\sigma$ and permittivity $\epsilon$ of the tissue can be obtained from $\hat{\epsilon}(\omega)$

$$\sigma(\omega) = -\omega\epsilon_0 \,\mathrm{Im}(\hat{\epsilon}(\omega)), \tag{5}$$

$$\epsilon(\omega) = \epsilon_0 \,\mathrm{Re}(\hat{\epsilon}(\omega)). \tag{6}$$

Biological tissues are naturally inhomogeneous, due to their complex macroscopic and microscopic structure, function and physiological condition. To account for this, the uncertainty level of the estimates from the above equations was set to ±20% following reported results in Gabriel *et al* (1996a).

The Electrical properties of BO were modelled as the average between cortical and cancellous bones, while OT was modelled as muscle tissue.

*2.1.2. Atlas statistics computation*

Let $\boldsymbol{u} \in \mathbb{R}^{N_V}$ be a vector representing a 3D image of the human head after normalization and segmentation, where $N_V$ is the number of voxels, excluding those representing the background around the head. Let the image be segmented into $N_T$ nonintersecting regions (tissues), each one with associated characteristic function $\boldsymbol{\chi}_t \in \mathbb{R}^{N_V}$, for $t = 1, 2, \cdots, N_T$. Also, let $p_t$ be the electrical property of each tissue under consideration. The property can be real (e.g. resistivity or conductivity) or complex-valued (e.g. impeditivity or admitivity). We can write the 3D image of this property $\boldsymbol{x} \in \mathbb{C}^{N_V}$ (or real with the same dimension) as

$$\boldsymbol{x} = \sum_{t=1}^{N_T} p_t \boldsymbol{\chi}_t = \boldsymbol{X}\boldsymbol{p}, \tag{7}$$

where $\boldsymbol{p} \in \mathbb{C}^{N_T}$ is a vector composed by the electrical properties of the tissues and $\boldsymbol{X} \in \mathbb{R}^{N_V \times N_T}$ is a matrix where each column is a characteristic function.

Assume images from $N_I$ individuals are used to build the atlas. Formally this number should be very large to represent the statistics of the population. In practice, this number is limited by the size of the dataset. To reduce this limitation each individual will be considered $N_S$ times, each time with a different value for $\boldsymbol{p}$, following the statistics of the tissues. This implies that the $N_I$ individuals represent the general shape of the head of the population while allowing the electrical properties of the tissues to be more diverse. In addition, we assume the same number of samples $N_S$ per individual, making them equally probable.

Using these hypotheses the average and covariance of the population can be estimated efficiently. For the covariance matrix $\boldsymbol{\Gamma}$ in special, the formulation allows the computation in factorized form $\boldsymbol{\Gamma} = \boldsymbol{K}\boldsymbol{K}^{\mathrm{T}}$, reducing storage requirements and simplifying algorithms that depend on factorizations of $\boldsymbol{\Gamma}$.

Samples of the $i$th individual can be composed by sampling the properties of the tissues $\boldsymbol{p}_s$ and applying (7)

$$\boldsymbol{x}_{s,i} = \boldsymbol{X}_i \boldsymbol{p}_s, \quad \text{for} \quad s = 1, 2, \cdots, N_S, \tag{8}$$

where the samples $\boldsymbol{p}_s$ can be generated from data fitted models or measurements. In this work, the electrical properties of the tissues are considered Gaussian with average resulting from the model (4) and standard deviation of 20% of the average, following reported results (Gabriel *et al* 1996a).

Let $\boldsymbol{x}_{s,i}$ represent a sample of the $i$th individual. The average over all individuals can be estimated with

$$\bar{x} = \frac{1}{N_S N_I} \sum_{i=1}^{N_I} \sum_{s=1}^{N_S} \boldsymbol{x}_{s,i} = \frac{1}{N_I} \sum_{i=1}^{N_I} \boldsymbol{X}_i \frac{1}{N_S} \sum_{s=1}^{N_S} \boldsymbol{p}_s = \frac{1}{N_I} \sum_{i=1}^{N_I} \boldsymbol{X}_i \bar{p}, \tag{9}$$

where, again, $N_S$ is fixed and represent the number of samples with the same head geometry $\boldsymbol{X}_i$ and $\bar{p}$ is the average electrical properties of the tissues.

The covariance matrix can be computed using the usual sample estimator

$$\boldsymbol{\Gamma} = \frac{1}{N_I N_S - 1} \sum_{i=1}^{N_I} \sum_{s=1}^{N_S} (\boldsymbol{x}_{s,i} - \bar{x})(\boldsymbol{x}_{s,i} - \bar{x})^{\mathrm{H}}, \tag{10}$$

where $\boldsymbol{\Gamma} \in \mathbb{R}^{N_V \times N_V}$ and $\boldsymbol{M}^{\mathrm{H}}$ denotes conjugate transpose of $\boldsymbol{M}$. For real valued $\boldsymbol{p}$, the conjugate transpose is the transpose $\boldsymbol{M}^{\mathrm{H}} = \boldsymbol{M}^{\mathrm{T}}$

Adding $(\bar{x}_i - \bar{x}_i)$ to both terms between parenthesis and rearranging the terms,

$$\boldsymbol{\Gamma} = \frac{1}{N_I N_S - 1} \sum_{i=1}^{N_I} \sum_{s=1}^{N_S} [(\boldsymbol{x}_{s,i} - \bar{x}_i) + (\bar{x}_i - \bar{x})][(\boldsymbol{x}_{s,i} - \bar{x}_i)^{\mathrm{H}} + (\bar{x}_i - \bar{x})^{\mathrm{H}}], \tag{11}$$

where $\bar{x}_i = \sum_{s=1}^{N_S} \boldsymbol{x}_{s,i}/N_S$ is the average of the $i$th individual. Proceeding with the products,

$$\boldsymbol{\Gamma} = \frac{1}{N_I N_S - 1} \sum_{i=1}^{N_I} (\alpha_1 + \alpha_2 + \alpha_3 + \alpha_4), \tag{12}$$

$$\alpha_1 = \sum_{s=1}^{N_S} (\boldsymbol{x}_{s,i} - \bar{x}_i)(\boldsymbol{x}_{s,i} - \bar{x}_i)^{\mathrm{H}} = (N_S - 1)\boldsymbol{\Gamma}_i, \tag{13}$$

$$\alpha_2 = \sum_{s=1}^{N_S}(\boldsymbol{x}_{s,i} - \bar{x}_i)(\bar{x}_i - \bar{x})^{\mathrm{H}} = \left[\sum_{s=1}^{N_S}(\boldsymbol{x}_{s,i} - \bar{x}_i)\right](\bar{x}_i - \bar{x})^{\mathrm{H}} = 0, \tag{14}$$

$$\alpha_3 = \sum_{s=1}^{N_S}(\bar{x}_i - \bar{x})(\boldsymbol{x}_{s,i} - \bar{x}_i)^{\mathrm{H}} = (\bar{x}_i - \bar{x})\left[\sum_{s=1}^{N_S}(\boldsymbol{x}_{s,i} - \bar{x}_i)^{\mathrm{H}}\right] = 0, \tag{15}$$

$$\alpha_4 = \sum_{s=1}^{N_S}(\bar{x}_i - \bar{x})(\bar{x}_i - \bar{x})^{\mathrm{H}} = N_S(\bar{x}_i - \bar{x})(\bar{x}_i - \bar{x})^{\mathrm{H}}. \tag{16}$$

Finally, taking the limit $N_S \to \infty$

$$\boldsymbol{\Gamma} = \frac{1}{N_I}\sum_{i=1}^{N_I}\boldsymbol{\Gamma}_i + \frac{1}{N_I}\sum_{i=1}^{N_I}(\bar{x}_i - \bar{x})(\bar{x}_i - \bar{x})^{\mathrm{H}}. \tag{17}$$

Defining $\Delta\bar{x}_i = \bar{x}_i - \bar{x}$ and observing the linear relation (7) we can rewrite this last expression as

$$\boldsymbol{\Gamma} = \frac{1}{N_I}\sum_{i=1}^{N_I}[\boldsymbol{X}_i\boldsymbol{\Gamma}_p\boldsymbol{X}_i^{\mathrm{H}} + \Delta\bar{x}_i\Delta\bar{x}_i^{\mathrm{H}}] = \sum_{i=1}^{N_I}\boldsymbol{W}_i\boldsymbol{W}_i^{\mathrm{H}}, \tag{18}$$

$$\boldsymbol{W}_i = \frac{1}{\sqrt{N_I}}\left[\boldsymbol{X}_i\sqrt{\boldsymbol{\Gamma}_p} \quad \Delta\bar{x}_i\right], \tag{19}$$

where $\boldsymbol{W}_i \in \mathbb{C}^{N_V\times(N_T+1)}$ and $\boldsymbol{\Gamma}_p \in \mathbb{C}^{N_T\times N_T}$ is the covariance matrix of the electrical properties of the tissues. Furthermore, the expression can be simplified to

$$\boldsymbol{\Gamma} = [\boldsymbol{W}_1 \ \cdots \ \boldsymbol{W}_I]\begin{bmatrix}\boldsymbol{W}_1^{\mathrm{H}}\\ \vdots \\ \boldsymbol{W}_I^{\mathrm{H}}\end{bmatrix} = \boldsymbol{K}\boldsymbol{K}^{\mathrm{H}}, \tag{20}$$

where $\boldsymbol{K} \in \mathbb{C}^{N_V\times[(N_T+1)N_I]}$. Note that both the average (9) and the covariance (20) estimates do not require explicit sampling procedure presented in (8).

In case of complex-valued $\boldsymbol{p}$, the pseudo-covariance $\tilde{\boldsymbol{\Gamma}} \in \mathbb{C}^{N_V\times N_V}$ can be computed in a similar way

$$\tilde{\boldsymbol{\Gamma}} = \boldsymbol{K}\boldsymbol{K}^{\mathrm{T}}. \tag{21}$$

The atlas in this work is assumed Gaussian, therefore $\bar{x}$ and $\boldsymbol{\Gamma}$ (and $\tilde{\boldsymbol{\Gamma}}$ for complex-valued $\boldsymbol{p}$) completely specify its probability density function.

### 2.2. Dynamic component

Flow in the cranial cavity is pulsatile, following the cardiac cycle. Arterial blood flows in waves, forcing part of the venous blood and CSF to move, following the Monro-Kellie hypothesis (Wagshul *et al* 2011). Venous blood is drained to the jugular veins via cerebral sinuses, while CSF moves in the subarachnoid space and leaves/returns to the cavity via the foramen magnum to balance intracranial pressure waves during the cardiac cycle (Greitz *et al* 1992, Sakka *et al* 2011). Recently, pulsatility was also observed in small cortical veins (Driver *et al* 2020), and studies in rats show that the flow in microvessels is quasi-steady laminar flow, following Hagen–Poiseuille law expected in low Reynolds and Womersley numbers (Seki *et al* 2006).

Arterial blood enters the cranial cavity through its base via two pairs of arteries, the (right/left) vertebral and internal carotid arteries. After entering, these arteries form the circle of Willis, a circulatory anastomosis responsible for providing backup routes for cerebral blood supply (Bradac 2017, Chandra *et al* 2017). From the circle of Willis four main pairs of arteries branch out, the (right/left) anterior, middle, posterior cerebral, and superior cerebellar arteries.

The dynamic component of the atlas comprises the circulation in the main cerebral arteries. The procedure follows the same main steps presented in section 2.1 with a few modifications. (i) Magnetic Resonance Angiography (MRA) images of 109 healthy human individuals were used (Bullitt *et al* 2005). The images were obtained in a three tesla equipment with a resolution of $0.5 \times 0.5 \times 0.8$ mm. An equal number of male and female individuals were used, with an average age of $43 \pm 14$ years old. (ii) Segmentation was performed first by applying a total variation filter to the images followed by a threshold segmentation. Only the lumen of the vessels with contrast agent were segmented. (iii) Electrical property assignment follows the procedure described in the following subsection.

#### *2.2.1. Electrical properties of the segments*

The influence of blood flow centre-line velocity and vessel radius over the electrical impedance of blood is modelled and included in the atlas (Gaw *et al* 2008, Shen *et al* 2016, 2018).

We simulated blood flow in the main arteries of the brain using the openBF solver (Melis *et al* 2017, Melis 2018), a 1D blood flow solver based on monotonic upstream-centered scheme for conservation laws

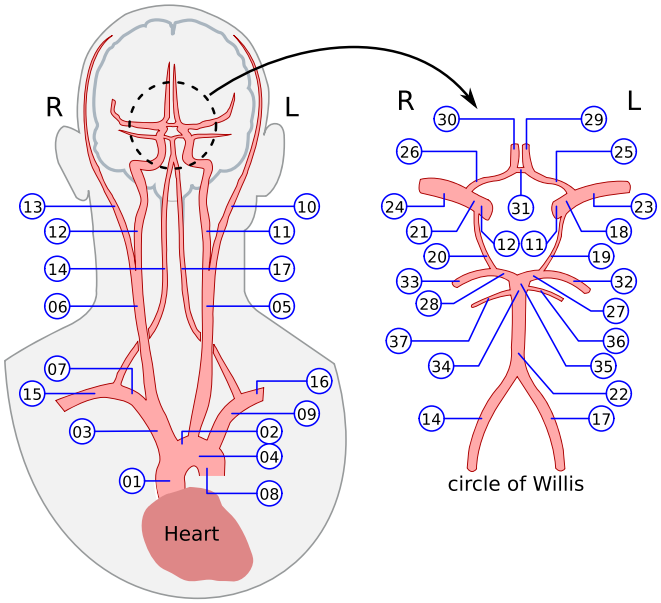


**Figure 3.** Superior aortic system considered in the simulations. The names of the vessels are presented in table 1.

(MUSCL) finite-volume numerical scheme. The solver assumes the blood is an incompressible Newtonian fluid, flowing through narrow and long circular vessels with linear compliant walls. The Navier–Stokes equations are reduced to 1D by imposing axisymmetry, linearized and solved for pulsatile flows using the finite difference method. Detailed description can be found in Melis (2017).

Brain circulation simulation encompasses the superior aortic system, from the ascending aorta to the main arteries providing blood to the brain. The arteries considered in the simulation can be seen in figure 3.

Blood was assumed Newtonian with density $\rho = 1050\ \mathrm{kg\ m^{-3}}$ and dynamic viscosity $\mu = 4.5 \times 10^{-3}$ Pa s. The geometry and mechanical properties of the vessels are presented in table 1, based on Alastruey *et al* (2007) and complemented with data collected by Dodo *et al* (2020), Fomkina *et al* (2016), Schmitter *et al* (2013). The terminal vessels were coupled with 3-element Windkessel models to mimic the perfusion of downstream vessels and avoid numerical oscillations. Heart flow output in one cardiac cycle was set to

$$Q(t) = \begin{cases} Q_M \sin\left(\dfrac{\pi t}{\tau}\right) & t < \tau \\ 0 & \text{otherwise} \end{cases}, \tag{22}$$

where $Q_M = 485\ \mathrm{ml\ s^{-1}}$ is peak flow rate, $\tau = 0.3$ s and the cardiac cycle period is 1 s, following (Alastruey *et al* 2007).

Lasting one cardiac cycle, the simulated pulsatile blood flow of each vessel must be converted to the electrical property of interest. Visser's model, a nonlinear function that relates blood resistivity changes to the average blood velocity in a cylindrical vessel, can be used for this purpose (Visser 1989, 1992, Hoetink *et al* 2004)

$$\frac{\Delta\rho_\ell}{\rho_0} = -0.45H\left[1 - \exp\left(-0.26\left|\frac{\bar{v}}{R}\right|^{0.39}\right)\right], \tag{23}$$

where $\Delta\rho_\ell$ is the longitudinal resistivity change to the reference (still blood) resistivity $\rho_0$, $H$ is the hematocrit (volume percentage of red blood cells in the blood), $\bar{v}$ is the average cross-sectional velocity and $R$ is the radius of the vessel. Visser's model presents a similar expression for the conductivity, however no expression was derived for other electrical properties. We will hypothesize the conductivity expression can be applied to the permittivity of blood.

Visser's model applies to blood flowing in a rigid vessel and in a defined orientation. Measurements taken from impedance cardiography studies in humans showed relative variations $\Delta\rho_\ell/\rho_0$ smaller (15% maximum) than predicted from Visser's model in the same conditions (25% maximum), 60% reduction (Raaijmakers *et al* 1996). The difference can be explained by the fact that the vessels are not straight and have different orientations. To accommodate this discrepancy, changes in blood resistivity were scaled to 60% of Visser's model (23), as reported in the literature.

For each time step, the electrical property of the blood in each main artery is calculated using Visser's model and used to compute the statistics of the atlas at that time instant.

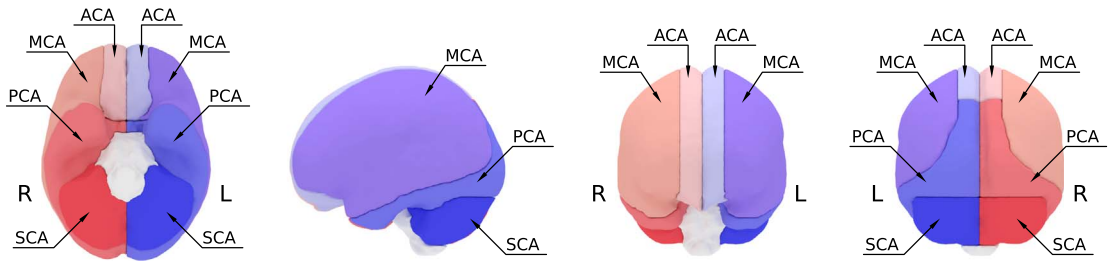


**Figure 4.** Main cerebral vascular territories. Acronyms: anterior cerebral artery (ACA), middle cerebral artery (MCA), posterior cerebral artery (PCA), superior cerebellar artery (SCA).

**Table 1.** Geometrical and mechanical properties of the arteries. Based on Alastruey *et al* (2007) and complemented with data collected by Dodo *et al* (2020), Fomkina *et al* (2016), Schmitter *et al* (2013). $\ell$: length, $r_0$: Proximal lumen radius, $E$: Young's modulus, $R_T$: Terminal resistance, and $C_T$: Terminal capacitance.

| # | Artery[a] | $\ell$ (mm) | $r_0$ (mm) | $E$ (kPa) | $R_T$ ($10^9$ Pa s m$^{-3}$) | $C_T$ ($10^{-10}$ m$^3$ Pa$^{-1}$) |
|---|---|---|---|---|---|---|
| 01 | Ascending aorta | 40 | 12.00 | 400 | — | —- |
| 02 | Aortic arch I | 20 | 11.20 | 400 | — | —- |
| 03 | Brachiocephalic | 34 | 6.20 | 400 | — | —- |
| 04 | Aortic arch II | 39 | 10.70 | 400 | — | —- |
| 05 | L CCA | 208 | 2.50 | 400 | — | —- |
| 06 | R CCA | 177 | 2.50 | 400 | — | —- |
| 07 | R Subclavian | 34 | 4.23 | 400 | — | —- |
| 08 | Thoracic aorta | 156 | 9.99 | 400 | 0.18 | 38.7 |
| 09 | L Subclavian | 34 | 4.23 | 400 | — | —- |
| 10/13 | ECA | 177 | 1.50 | 800 | 5.43 | 1.27 |
| 11/12 | ICA I | 177 | 2.00 | 800 | — | —- |
| 14/17 | Vertebral | 148 | 1.36 | 800 | — | —- |
| 15/16 | Brachial | 422 | 4.03 | 400 | 2.68 | 2.58 |
| 18/21 | ICA II | 5 | 2.00 | 1600 | — | —- |
| 19/20 | PCoA | 15 | 0.73 | 1600 | — | —- |
| 22 | Basilar I | 25 | 1.62 | 1600 | — | —- |
| 23/24 | MCA | 119 | 1.43 | 1600 | 5.97 | 1.16 |
| 25/26 | ACA I | 12 | 1.17 | 1600 | — | —- |
| 27/28 | PCA I | 5 | 1.07 | 1600 | — | —- |
| 29/30 | ACA II | 103 | 1.20 | 1600 | 8.48 | 0.82 |
| 31 | ACoA | 3 | 0.74 | 1600 | — | —- |
| 32/33 | PCA II | 86 | 1.05 | 1600 | 11.08 | 0.62 |
| 34 | Basilar II | 1 | 1.62 | 1600 | — | —- |
| 35 | Basilar III | 3 | 1.62 | 1600 | — | —- |
| 36/37 | SCA | 86 | 0.65 | 1600 | 25.0 | 0.62 |

[a] Acronyms:Anterior cerebral artery (ACA), Anterior communicating artery (ACoA), Common carotid artery (CCA), External carotid artery (ECA), Internal carotid artery (ICA), Middle cerebral artery (MCA), Posterior cerebral artery (PCA), Posterior communicating artery (PCoA), Superior cerebellar artery (SCA).

The volume occupied by the main arteries is small compared to the volume of the brain, however its area of influence is considerable. Each artery is responsible for providing blood to specific areas of the brain, known as brain arterial vascular territories (Kim *et al* 2019). Six main supratentorial vascular territories were modelled, (right/left) MCA, ACA, and PCA, also the (right/left) superior cerebellar artery. The main brain territories can be seen in figure 4. In addition to these, the (right/left) external carotid territories were also included due to the proximity to the electrodes that can impact measurements. The dynamic model does not consider collateral circulation other than the redundancy coming from the circle of Willis.

Blood supply inside each territory is assumed to be proportional to the waveform of the associated main artery. To the best of our knowledge, there are not many studies on electrical property variations of brain tissues along the cardiac cycle. The majority of the studies focus on electrical property changes in response to sensorial or motor activity or epilepsy events (Newell *et al* 2002, Tidswell *et al* 2001, Towers *et al* 2000, Holder *et al* 1996). The net electrical property change is caused by a dynamic balance between the amount of blood, extracellular

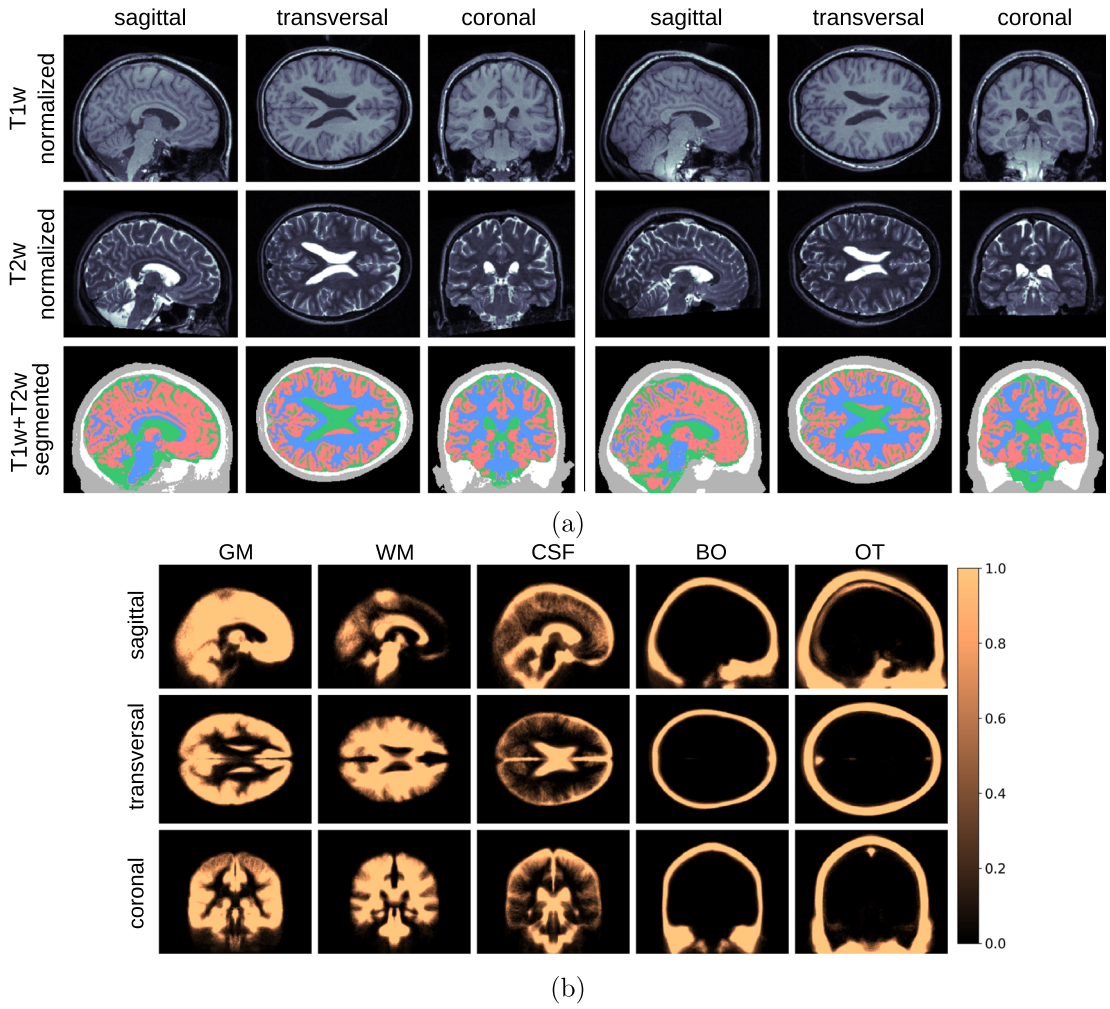


**Figure 5.** Static atlas computations. (a) Processing steps of two representative individuals of the dataset. The first two row shows T1w and T2w images after normalization and the third row the result SPM's multi-channel segmentation (T1w+T2w). GM: red, WM: blue, CSF: green, BO: white, and OT: grey. (b) Average of the characteristic functions $\chi_t$ for each tissue.

fluids, and cell swelling in a given location and at a given time instant. In this study, the dynamic component of this variation is set to 0.5% of the main artery of the territory (Tidswell *et al* 2001).

### *2.2.2. Atlas statistics computation*

Based on the segmentation of the vessels, explained in section 2.2, and the location of the vascular territories, presented in figure 4, it is possible to define two characteristic functions per territory, the main vessels in a given territory $\boldsymbol{\chi}_m \in \mathbb{R}^{N_V}$ and its area of influence $\boldsymbol{\chi}_m^c \in \mathbb{R}^{N_V}$ (the complement within the vascular territory).

Let $N_M$ be the number of vascular territories. We can write a 3D image of the electrical property of the dynamic component $\boldsymbol{x}(t) \in \mathbb{C}^{N_T}$ as

$$\boldsymbol{x}(t) = \sum_{m=1}^{N_M} p_{m,B}(t)\boldsymbol{\chi}_m + p_{m,B}^c(t)\boldsymbol{\chi}_m^c, \tag{24}$$

where $p_{m,B}(t)$ and $p_{m,B}^c(t)$ are the electrical properties of blood in the respective segments. The effect of blood in the complements $p_{m,B}^c(t)$ is modelled as a percentage of $p_{m,B}(t)$

$$\boldsymbol{x}(t) = \sum_{m=1}^{N_M} p_{m,B}(t)(\boldsymbol{\chi}_m + \alpha_m\boldsymbol{\chi}_m^c) = \sum_{m=1}^{N_M} p_{m,B}(t)\boldsymbol{\chi}_{\alpha,m}, \tag{25}$$

where $\alpha_m \geqslant 0$ adjusts the effect. The vector $\boldsymbol{\chi}_{\alpha,m}$ represents the influence region of each vascular territory and can be used to compose images as in (7). The statistics of the dynamic component is computed following the same procedure presented in section 2.1.2 with the modified characteristic function $\boldsymbol{\chi}_{\alpha,m}$.

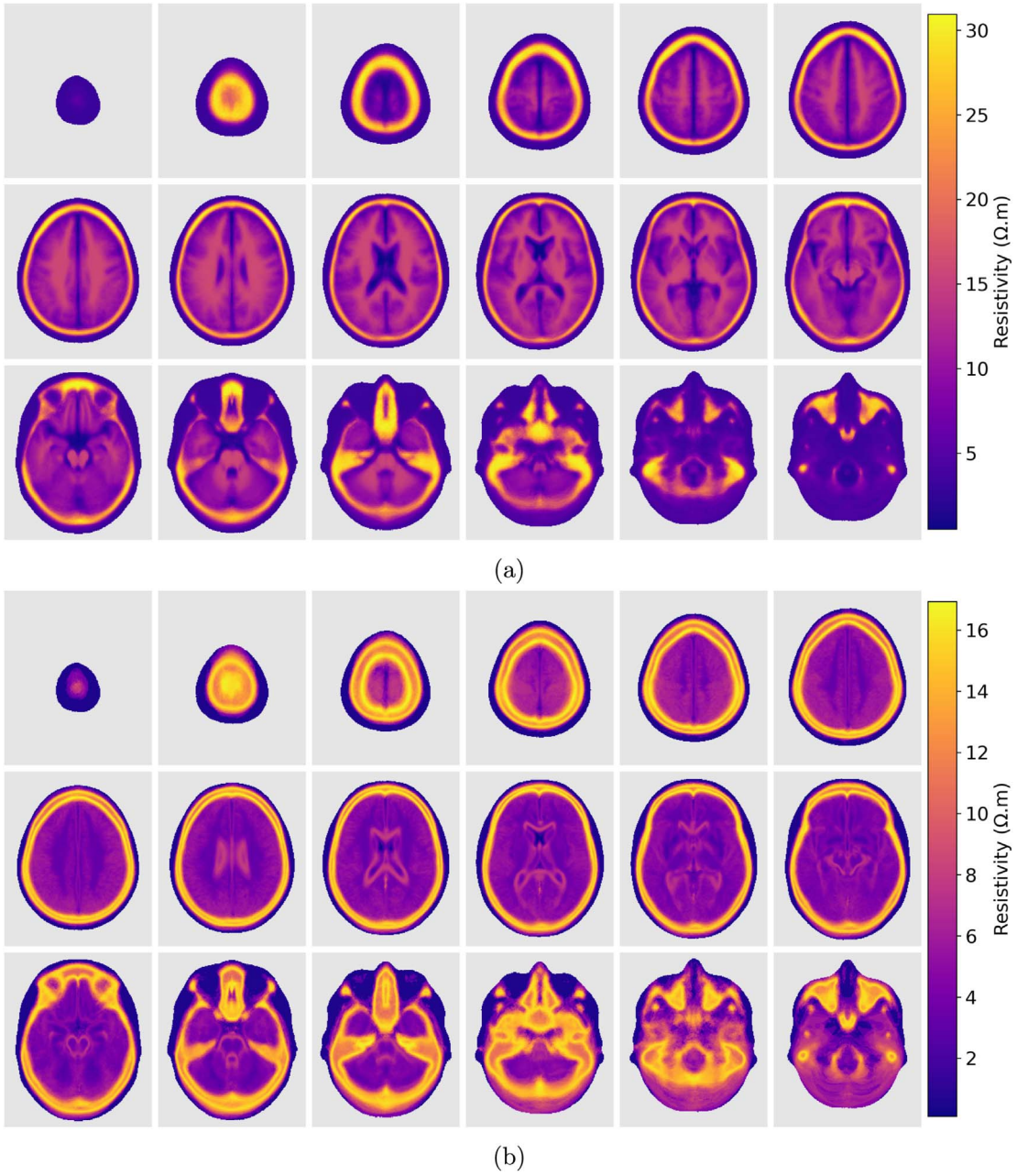


**Figure 6.** Transversal slices of the static component of the atlas (resistivity) at 1 kHz. (a) average; (b) standard deviation.

## 3. Results

### 3.1. Static component of the atlas

Figure 5(a) shows two representative individuals in the segmentation steps to compute the static component of the atlas. The first two rows present T1w and T2w images after normalization and the third row show the segmented tissues using SPM's multi-channel segmentation (T1w+T2w). Figure 5(b) shows the average over the characteristic functions of all individuals and for each segmented tissue. A voxel with a value equal to 1.0 indicates it was classified as the same tissue across all subjects.

The static component of the atlas at 1 kHz is presented in figure 6. The figure shows transversal slices of the average (figure 6(a)) and standard deviation (figure 6(b)). It is possible to see high resistivity regions in the forehead, caused by the thick bone and the frontal sinus, in the zygomatic bones and the petrous part of the temporal bone in the base of the skull.

Figure 7 shows slices of the atlas built in terms of conductivity, resistivity, and relative permittivity in different frequencies. The figure shows that the average resistivity and permittivity decrease with increases in frequency while conductivity increases. Although the average process tends to eliminate small features of the

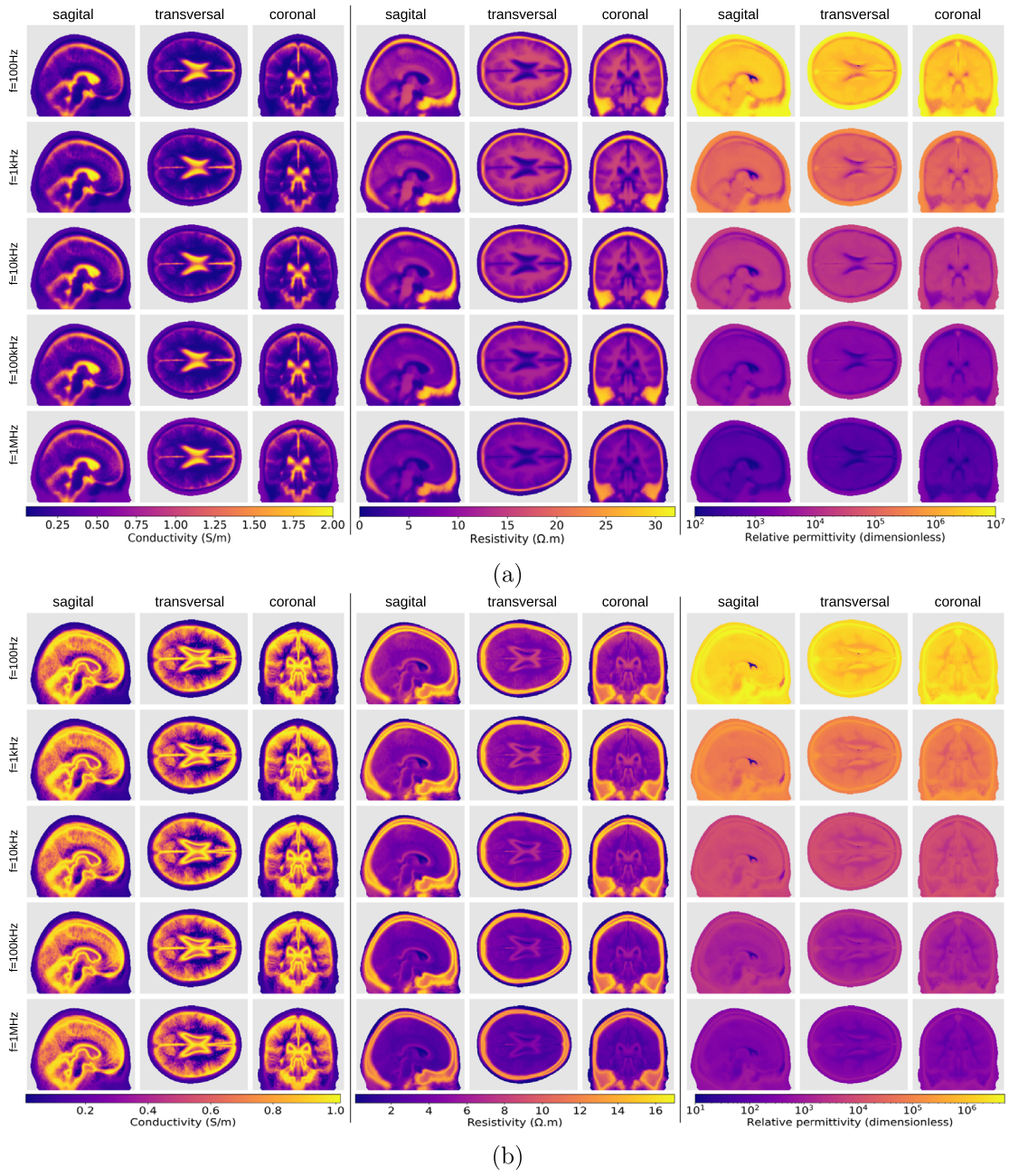


**Figure 7.** Statistics of the atlas in different frequencies. (a) Average; (b) standard deviation.

images, it is still possible to see small and thin structures inside the brain, like the longitudinal fissure, third and fourth ventricles and central canal.

### 3.2. Dynamic component

The dynamic component of the atlas was computed following the procedure described in section 2.2. Transversal slices of the average at 1 kHz are presented in figure 8. The main vessels that compose the circle of Willis in the base of the cranial cavity, the dense arterial vascularization in the insular cortex, and the superior sagittal sinus are visible.

Figure 9 presents the waveforms obtained from the Navier–Stokes solver simulating one cardiac cycle (60 bpm), with hematocrit $H = 0.5$. From left to right, the figure presents flow rate, average cross-sectional velocity, static pressure and resistivity changes to still blood following Visser's model (23). Peak velocity occurs approximately 0.25 s after the beginning of the cardiac cycle. Resistivity changes lie within −17% and −21% to still blood, indicating the resistivity in these vessels differs considerably from the electrical properties of still blood.

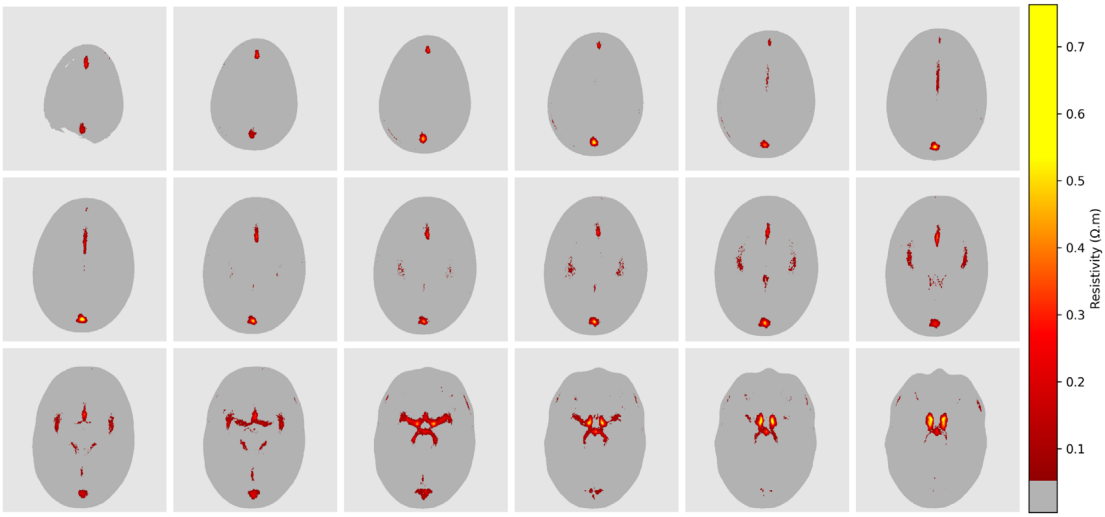


**Figure 8.** Transversal slices of the average image of the segmented vessels filled with still blood at 1 kHz. Small values were masked in grey to emphasize the structure of the main vessels.

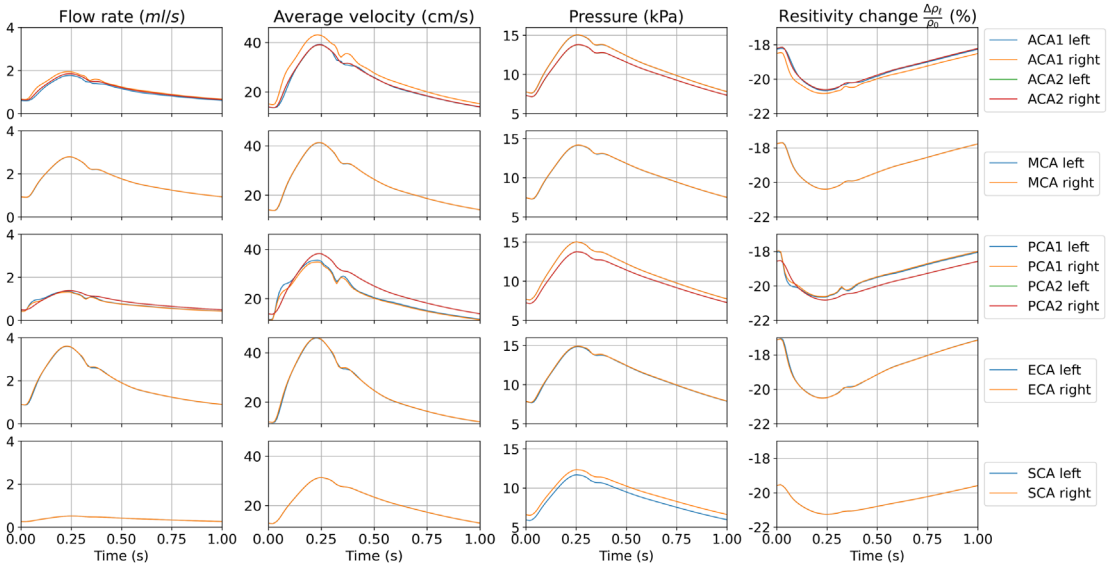


**Figure 9.** Waveforms of the main arteries over one cardiac cycle. From left to right: flow rate, average cross-sectional velocity, static pressure and resistivity changes.

### 3.3. Effects of the cardiac cycle on surface measurements for electrical impedance tomography

As one example of application, the atlas was employed to simulate EIT surface electrode measurements at 1 kHz during one cardiac cycle (60 bpm) using the FEM to solve the complete electrode model for EIT (Cheney *et al* 1999, Holder 2005). This type of *in silico* study is important to investigate the possibility of monitoring blood perfusion anomalies in patients.

A segmented head image of an average young adult[4] was selected to create the geometry (Hammond *et al* 2017, Hou *et al* 2017, Song *et al* 2013). This geometry is not among those used to create the atlas, avoiding statistical biases. The boundary surfaces of the segments were extracted and cleaned to remove artefacts.

A FEM mesh was created using Gmsh software (Geuzaine and Remacle 2009). The mesh, presented in figure 10(a), is composed of 2.06 million linear tetrahedral elements, split into six segments and 32 electrodes with diameter of 15 mm were placed in two parallel planes with 20 mm of separation. Electrode numbers can be seen in the figure.

The atlas was projected into the FEM mesh using the SyN (Avants *et al* 2008). The method requires two 3D binary images with the characteristic functions of the same volume, one in the atlas reference system and one in

[4] https://pedeheadmod.net/pediatric-head-atlases/

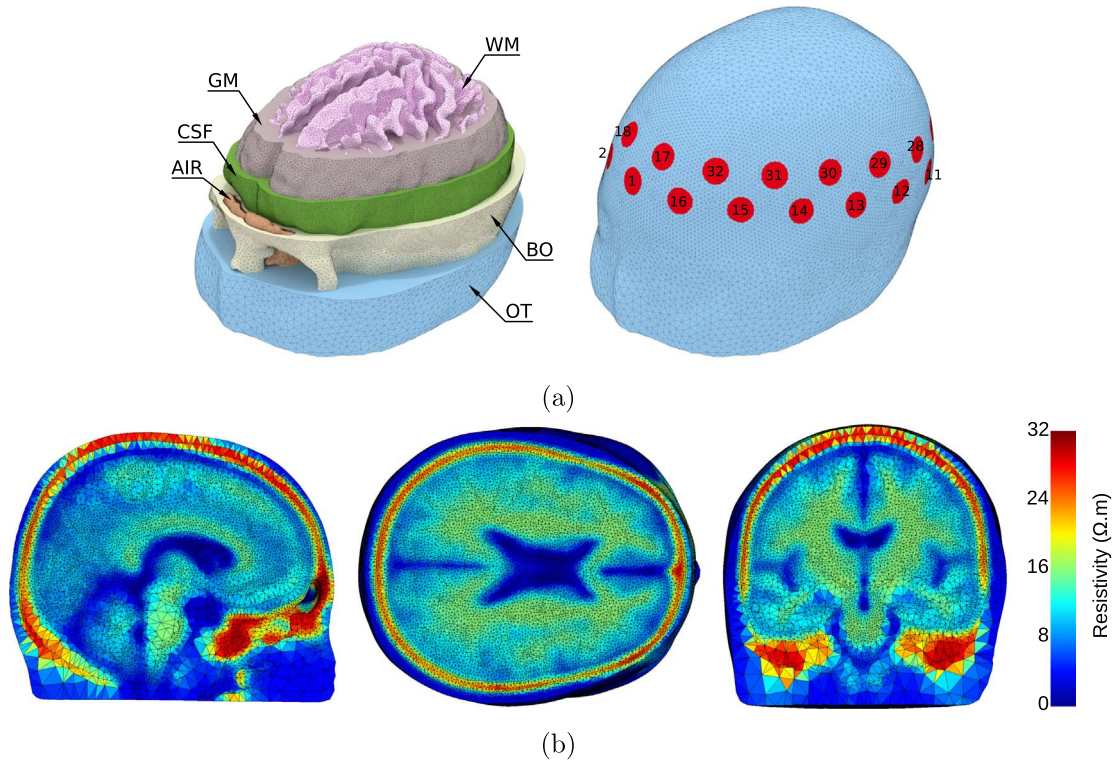


**Figure 10.** Finite element mesh used to simulate EIT measurements. (a) Internal structure and electrode locations; (b) slices of the projected atlas into the FEM mesh.

the FEM mesh reference system. The volumes used for the normalization comprise the soft tissues inside the cranial cavity (CC=GM+WM+CSF).

For the atlas, the characteristic function of the cranial cavity $\boldsymbol{\chi}_{CC}$ is found by taking the average of the sum of the characteristic functions of these tissues over all individuals that compose the atlas, followed by thresholding at 75%

$$\bar{\chi} = E\{\boldsymbol{\chi}_{WM} + \boldsymbol{\chi}_{GM} + \boldsymbol{\chi}_{CSF}\}, \tag{26}$$

$$\boldsymbol{\chi}_{CC}(i, j, k) = \begin{cases} 1 & \text{if } \bar{\chi}(i, j, k) \geqslant 0.75 \\ 0 & \text{otherwise} \end{cases}, \tag{27}$$

where $(i, j, k)$ is the coordinates of each voxel. For the FEM mesh, a 3D image can be created from the segmented internal structures of the mesh, seen in figure 10(b), by defining a 3D grid of points that encloses the head and checking if each voxel belongs to the cranial cavity segment CC.

The affine transformation resulting from the normalization was applied to all voxels of the atlas, projecting them into the FEM mesh reference system. Finally, the values of the atlas were interpolated into the centroids of the tetrahedron. The projection can be seen in figure 10(b).

EIT measurement simulation was performed by imposing sinusoidal bipolar current injection of 1 mA at 1 kHz and computing the electrode voltage measurements. Current pattern follows a skip-8 scheme to allow diametral current injection (two planes with 16 electrodes each) (Silva *et al* 2017). This choice mitigates the electrical shunting effect of the skull that causes the majority of the current to flow along the scalp only if the pair of injecting electrodes are too close. The simulated measurements are presented in figure 11 in four time instants along the cardiac cycle.

Figure 11(a) presents the measurements at $t = 0$s, used as reference measurement $\boldsymbol{v}_0$. Figure 11(b) shows relative differences $\Delta\boldsymbol{v}(t)$, in dB, between measurements in three other time instants $\boldsymbol{v}(t)$ and the reference $\boldsymbol{v}_0$, defined as

$$\Delta\boldsymbol{v}(t) = 20\log_{10}\left(\left|\frac{\boldsymbol{v}(t) - \boldsymbol{v}_0}{\boldsymbol{v}_0}\right|\right), \tag{28}$$

where the division is computed element-wise. Figure 11(c) is a plot of the same differences for the first 32 measurements and show that the largest differences are measured at $t = 0.25$ s, time instant when we have peak velocities, as presented before in figure 9. Figure 11(d) presents histograms of the differences $\Delta\boldsymbol{v}(t)$. In the same

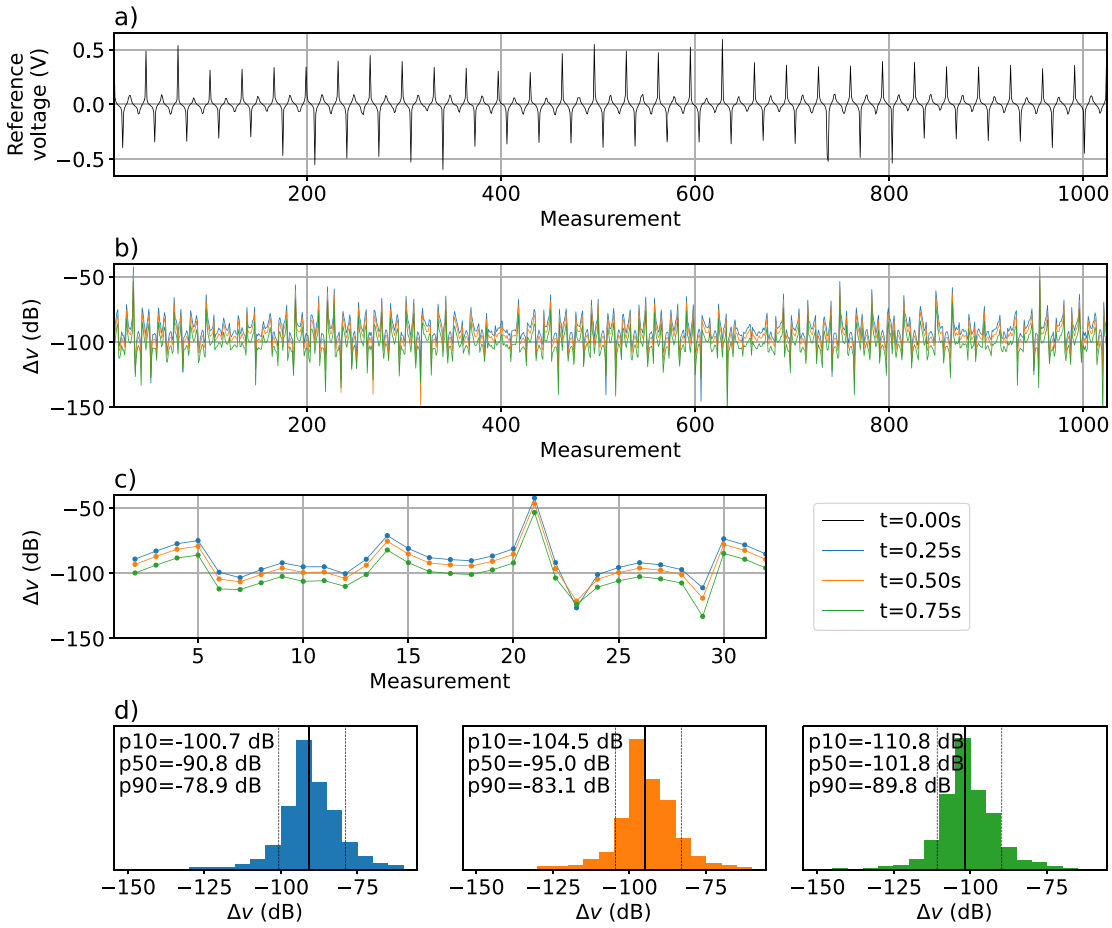


**Figure 11.** Simulated electrode measurements. (a) Reference measurements $\boldsymbol{v}_0$; (b) relative differences $\Delta\boldsymbol{v}(t)$; (c) first 32 relative differences $\Delta\boldsymbol{v}(t)$; (d) histograms of the differences $\Delta\boldsymbol{v}(t)$.

histograms, the vertical lines represent the percentiles 10%, 50% (median), and 90% together with their numeric values (p10, p50, and p90).

## 4. Discussion

Conductor volume problems in electroencephalography and electrical bioimpedance cerebral monitoring require a 3D model of the head and its electrical properties for solving the associated PDEs numerically. In many situations, a 3D model of the head of the patient is not available or an average head model is preferred. Even in cases when the model is available via MRI or CT images, the electrical properties of the tissues might not be completely known due to natural variability. This work presents a novel 4D (3D+T) statistical anatomical atlas of the electrical properties of the human head for electrophysiology applications created from MRI images of 107 subjects.

Satisfactory skull segmentation was achieved by employing SPM's multi-channel MRI (T1w+T2w) segmentation (Nielsen *et al* 2018). For the atlas, T1w and T2w MRI images were used to segment the tissues. This choice resulted in good segmentation for the purpose of the atlas and reduced the number of artefacts compared with segmentation based only on T1 images, especially near the anterior part of the frontal bone. The relatively large number of subjects, 107 in total, also helps to mitigate the effects of eventual segmentation artefacts in the final statistics.

The atlas was built for an average head shape and can be normalized to specific geometries. This process was exemplified with one EIT application. The normalization step optimized the alignment of the cranial cavity, volume comprising GM+WM+CSF segments. In our experiments, this choice produces a better match between the atlas and the FEM mesh. However, this choice can cause small artefacts in the external surface of the mesh due to the small thickness of the scalp and its proximity to the skull. These artefacts can be seen in figure 10(b) where the resistivity of the scalp near the top of the cranial vault is affected by the skull.

The electrical properties of biological tissues are frequency dependent. The atlas can be built for different frequencies as exemplified in figure 7. This flexibility expands the applicability of the atlas, such as in multifrequency EIT (Horesh 2006, Malone *et al* 2014).

Cerebral circulation was also modelled and added to the atlas. The atlas is capable of simulating the pulsatile blood flow in the main cerebral arteries and vascular territories and their effects on electrical measurements. As one example of application, the atlas was employed in an *in silico* study to investigate the possibility of monitoring blood perfusion using EIT. Among other objectives, this type of study is important to provide information on measurement sensitivity necessary to detect perfusion anomalies and serve as a guide for future EIT equipment developments for these applications. Figure 11(d) predicts that EIT equipment need a signal-to-noise ratio between 100 and 125 dB to identify changes due to the cardiac cycle. This is in good agreement with a previous study (Towers *et al* 2000) on clamped carotid arteries.

Conductor volume inverse problems are sensitive to modelling errors. The skull encloses the brain, and its proximity to the surface and high resistivity imposes a strong barrier to electric current. In EIT, the skull causes the majority of the current to flow along the scalp and not penetrate the skull cavity. This shielding causes drop in sensitivity inside the the skull cavity. The high SNR ratio requirement obtained from the simulation is a direct consequence of the intense shielding effect of the skull. In EEG, the skull causes difficulties to measure brain activity due to the insulating effect and results in substantial errors in source localization problems. These difficulties reinforce the necessity of accurate geometric models of the skull and accurate priors of the skull for inverse problems in electrophysiology.

The statistical nature of the atlas also allows quantifying its uncertainty. Figure 6 shows that the regions with the largest standard variations are located along the boundary of the bones. This can be explained by the fact that small anatomical differences between the skulls of the individuals cause large resistivity variations due to the difference between the resistivity of bones and other tissues around them.

The proposed atlas has some limitations. It is known that ageing increases the stiffness of the vessels, however the atlas does not include ageing effects on the stiffness of the walls of the arteries. Nevertheless, the atlas can be adjusted by setting Young's modulus of the vessels accordingly with the age of the population. Except for the redundancy caused by the circle of Willis, collateral brain circulation was not modelled either caused by preexisting vascular redundancy or neovascularization. The venous side of the circulation was not modelled. Although only five main tissues were segmented, the method can be readily extended to accommodate more tissues. All tissues were modelled as isotropic, even though it is known that some tissues are anisotropic. Extending the atlas to anisotropic tissue is possible but increases the complexity substantially. Also, the scalp was modelled as a uniform tissue, however it is a multi-layer tissue, composed of skin, connective tissue, epicranial aponeurosis, and muscles that have different electrical properties. Due to its proximity to the electrodes, scalp mismodellings can impact EIT recovered images. Finally, the dynamic effect of blood circulation in each territory was modelled as proportional to the velocity of the blood in the main vessel. This approximation does not take into consideration variations in the volume of blood in a given region, for example when the brain responds to external stimuli. The current limitations of the atlas act as motivation for future research topics. These challenging limitation will be the focus of future works to further improve the anatomical atlas.

The atlas was developed in Python 3, and the source code is available at https://github.com/fsmMLK/openSAHE or archived at https://doi.org/10.5281/zenodo.5567086. The source code contains also the EIT forward problem solver and meshes used in this work. The atlases created in this work are also available precomputed at https://doi.org/10.5281/zenodo.5559624. Github repository contains a detailed description of the files, installation, and usage.

## 5. Conclusion

We presented a novel anatomical atlas of the electrical properties of the human head. To the best of our knowledge, the present model is the first model capable of simulating cerebral circulation and its effects on electrical measurements. Despite the limitations, the atlas brings important implications to cerebral electrophysiology studies. This novelty has the potential to become an important tool for *in silico* studies on cerebral circulation and electrophysiology, such as electrical measurement sensitivity to vascular pathologic conditions like stroke classification and monitoring, arterial vasospasms, and arteriovenous malformation. The atlas can also be used as statistical prior information for inverse problems in EEG and EIT and to create training sets for machine learning algorithms.

## Acknowledgments

The work was funded in part by the Jane and Aatos Erkko Foundation, project 'Electrical Impedance Tomography—a novel method for improved diagnosis of stroke', the Academy of Finland (Centre of Excellence in Inverse Modelling and Imaging, decision number 312 339), the São Paulo Research Foundation–FAPESP (Process numbers: 2019/09154-7 and 2017/18378-0) and Coordenação de Aperfeiçoamento de Pessoal de Nível Superior (CAPES)—Finance Code 001. The authors wish to thank the Finnish Grid and Cloud Infrastructure (FGCI) for supporting this project with computational and data storage resources.

The MR brain images from healthy volunteers used in this paper were collected and made available by the CASILab at The University of North Carolina at Chapel Hill and were distributed by the MIDAS Data Server at Kitware, Inc. (https://insight-journal.org/midas/community/view/21)

## ORCID iDs

Fernando S Moura https://orcid.org/0000-0002-0433-1224
Roberto G Beraldo https://orcid.org/0000-0001-6986-3435
Leonardo A Ferreira https://orcid.org/0000-0001-5303-2776
Samuli Siltanen https://orcid.org/0000-0002-5988-5232

## References

Acar Z A and Makeig S 2013 Effects of forward model errors on EEG source localization *Brain Topogr.* **26** 378–96
Adler A and Boyle A 2019 Electrical impedance tomography *Wiley Encyclopedia of Electrical and Electronics Engineering* ed J G Webster 2nd edn (New Jersey, NJ: Wiley) pp 1–16
Agnelli J P, Çöl A, Lassas M, Murthy R, Santacesaria M and Siltanen S 2020 Classification of stroke using neural networks in electrical impedance tomography *Inverse Problems* **36** 115008
Alastruey J, Parker K H and Peiró J 2007 Modelling the circle of willis to assess the effects of anatomical variations and occlusions on cerebral flows *J. Biomech.* **40** 1794–805
Andreuccetti D, Fossi R and Petrucci C 1997 An internet resource for the calcu lation of the dielectric properties of body tissues in the frequency range 10 hz - 100 ghz http://niremf.ifac.cnr.it/tissprop/
Ashburner J and Friston K 2005 Unified segmentation *Neuroimage* **26** 839–51
Avants B, Grossman C E M and Gee J 2008 Symmetric diffeomorphic image registration with cross-correlation: evaluating automated labeling of elderly and neurodegenerative brain *Med. Image Anal.* **12** 26–41
Avants B, Tustison N, Song G and Gee J 2009 Ants: open-source tools for normalization and neuroanatomy https://sourceforge.net/projects/advants/
Badeli V, Melito G M, Köstinger A R, Bíró O and Ellermann K 2020 Electrode positioning to investigate the changes of the thoracic bioimpedance caused by aortic dissection—a simulation study *J. Electr. Bioimpedance* **11** 38–48
Beraldo R G and Moura F S 2020 Time-difference electrical impedance tomography with a blood flow model as prior information for stroke monitoring *Proc. XXVII Brazilian Congress on Biomedical Engineering* (Vitória, Brazil: SBEB) pp 280–5
Bernstein D P 2010 Impedance cardiography: pulsatile blood flow and the biophysical and electrodynamic basis for the stroke volume equations *J. Electr. Bioimpedance* **1** 2–17
Bodo M, Montgomery L D, Pearce F J and Armonda R 2018 Measurement of cerebral blood flow autoregulation with rheoencephalography: a comparative pig study *J. Electr. Bioimpedance* **9** 123–32
Bradac G B 2017 *Vascular Territories* (Cham: Springer International Publishing) pp 105–7
Braun F, Proença M, Lemay M, Bertschi M, Adler A, Thiran J-P and Solà J 2018 Limitations and challenges of EIT-based monitoring of stroke volume and pulmonary artery pressure *Physiol. Meas.* **39** 014003
Bullitt E, Zeng D, Gerig G, Aylward S, Joshi S, Smith J K, Lin W and Ewend M G 2005 Vessel tortuosity and brain tumor malignancy: a blinded study *Acad. Radiol.* **12** 1232–40
Candiani V, Hannukainen A and Hyvonen N 2019 Computational framework for applying electrical impedance tomography to head imaging *SIAM J. Sci. Comput.* **41** B1034–60
Candiani V and Santacesaria M 2022 Neural networks for classification of strokes in electrical impedance tomography on a 3d head model *Mathematics in Engineering* **4** 1–22
Chandra A, Li W, Stone C, Geng X and Ding Y 2017 The cerebral circulation and cerebrovascular disease I: Anatomy *Brain Circ.* **3** 45–56
Cheney M, Isaacson D and Newell J C 1999 Electrical impedance tomography *SIAM Rev.* **41** 85–101
Cho J-H, Vorwerk J, Wolters C H and Knösche T R 2015 Influence of the head model on EEG and MEG source connectivity analyses *NeuroImage* **110** 60–77
Desmidt T, Andersson F, Brizard B, Dujardin P-A, Cottier J-P, Patat F, Réméniéras J-P, Gissot V, El-Hage W and Camus V 2018 Ultrasound measures of brain pulsatility correlate with subcortical brain volumes in healthy young adults *Ultrasound Med. Biol.* **44** 2307–13
Dodo Y, Takahashi T, Honjo K, Kitamura N and Maruyama H 2020 Measurement of the length of vertebrobasilar arteries: a three-dimensional approach *J. Neurol. Sci.* **414** 116818
Dowrick T, Blochet C and Holder D 2016 *In vivo* bioimpedance changes during haemorrhagic and ischaemic stroke in rats: towards 3d stroke imaging using electrical impedance tomography *Physiol. Meas.* **37** 765–84
Driver I D, Traat M, Fasano F and Wise R G 2020 Most small cerebral cortical veins demonstrate significant flow pulsatility: a human phase contrast mri study at 7t *Front. Neurosci.* **14** 415
Fomkina O A, Nikolenko V N and Chernyshkova E V 2016 Morphology and biomechanical properties of cerebellar arteries in adults *Russ. Open Med. J.* **5** e0205

Fonov V, Evans A, McKinstry R, Almli C and Collins D 2009 Unbiased nonlinear average age-appropriate brain templates from birth to adulthood *NeuroImage* **47** S102
Frackowiak R S, Friston K J, Frith C D, Dolan R J, Price C J, Zeki S, Ashburner J T and Penny W D 2004 Chapter 31—experimental design and statistical parametric mapping *Human Brain Function* 2nd edn (Burlington: Academic) pp 599–632
Frerichs I *et al* 2016 Chest electrical impedance tomography examination, data analysis, terminology, clinical use and recommendations: consensus statement of the TRanslational EIT developmeNt stuDy group *Thorax* **72** 83–93
Gabriel C, Gabriel S and Corthout E 1996 The dielectric properties of biological tissues: I. Literature survey *Physics Med. Biol.* **41** 2231–49
Gabriel S, Lau R W and Gabriel C 1996a The dielectric properties of biological tissues: II. Measurements in the frequency range 10 hz to 20 ghz *Phys. Med. Biol.* **41** 2251–69
Gabriel S, Lau R W and Gabriel C 1996b The dielectric properties of biological tissues: III. Parametric models for the dielectric spectrum of tissues *Phys. Med. Biol.* **41** 2271–93
Gaw R L, Cornish B H and Thomas B J 2008 The electrical impedance of pulsatile blood flowing through rigid tubes: a theoretical investigation *IEEE Trans. Biomed. Eng.* **55** 721–7
Geuzaine C and Remacle J F 2009 Gmsh: A 3-d finite element mesh generator with built-in pre- and post-processing facilities *Int. J. Numer. Methods Eng.* **79** 1309–31
Goren N, Avery J, Dowrick T, Mackle E, Witkowska-Wrobel A, Werring D and Holder D 2018 Multi-frequency electrical impedance tomography and neuroimaging data in stroke patients *Sci. Data* **5** 180112
Gorgolewski K, Burns C, Madison C, Clark D, Halchenko Y, Waskom M and Ghosh S 2011 Nipype: a flexible, lightweight and extensible neuroimaging data processing framework in python *Front. Neuroinform.* **5** 13
Grabner G, Janke A L, Budge M M, Smith D, Pruessner J and Collins D L 2006 Symmetric atlasing and model based segmentation: an application to the hippocampus in older adults *Medical Image Computing and Computer-Assisted Intervention–MICCAI 2006* ed R Larsen *et al* (Berlin, Heidelberg: Springer ) pp 58–66
Grech R, Cassar T, Muscat J, Camilleri K P, Fabri S G, Zervakis M, Xanthopoulos P, Sakkalis V and Vanrumste B 2008 Review on solving the inverse problem in eeg source analysis *J. NeuroEng. Rehabil.* **5** 25
Greitz D, Wirestam R, Franck A, Nordell B, Thomsen C and StÅhlberg F 1992 Pulsatile brain movement and associated hydrodynamics studied by magnetic resonance phase imaging *Neuroradiology* **34** 370–80
Hallez H *et al* 2007 Review on solving the forward problem in eeg source analysis *J. NeuroEng. Rehabil.* **4** 46
Hammond D, Price N and Turovets S 2017 *Construction and Segmentation of Pediatric Head Tissue Atlases for Electrical Head Modeling* (Vancouver, Canada: OHBM)
Hoetink A E, Faes T J C, Visser K R and Heethaar R M 2004 On the flow dependency of the electrical conductivity of blood *IEEE Trans. Biomed. Eng.* **51** 1251–61
Holder D S 2005 *Electrical Impedance Tomography: Methods, History and Applications* 1st edn (Cornwall, UK: IOP Publishing Ltd)
Holder D S, Rao A and Hanquan Y 1996 Imaging of physiologically evoked responses by electrical impedance tomography with cortical electrodes in the anaesthetized rabbit *Physiol. Meas.* **17** A179–86
Holmgren M, WÅhlin A, DunÅs T, Malm J and Eklund A 2019 assessment of cerebral blood flow pulsatility and cerebral arterial compliance with 4d flow MRI *J. Magn. Reson. Imaging* **51** 1516–25
Horesh L 2006 Some novel approaches in modelling and image reconstruction for multi-frequency electrical impedance tomography of the human brain *PhD Thesis* Department of Medical Physics—University College London
Hou J, Turovets S, Li K, Luu P, Tucker D and Larson-Prior L 2017 *Spatially Resolved Pediatric Skull Conductivities for Inhomogeneous Electrical Forward Modeling* (Vancouver, Canada: OHBM)
Jatoi M A and Kamel N 2017 *Brain Source Localization Using EEG Signal Analysis* (Boca Raton, FL: CRC Press)
Kaipio J and Somersalo E 2005 *Statistical and Computational Inverse Problems* (New York, NY: Springer)
Kim D-E, Jang J, Schellingerhout D, Ryu W-S, Park J-H, Lee S-K, Kim D and Bae H-J 2019 Supratentorial cerebral arterial territories for computed tomograms: a mapping study in 1160 large artery infarcts *Sci. Rep.* **9** 11708
Kneihsl M *et al* 2020 Intracranial pulsatility in relation to severity and progression of cerebral white matter hyperintensities *Stroke* **51** 3302–9
Kucewicz J C, Dunmire B, Giardino N D, Leotta D F, Paun M, Dager S R and Beach K W 2008 Tissue pulsatility imaging of cerebral vasoreactivity during hyperventilation *Ultrasound Med. Biol.* **34** 1200–8
Malone E, Jehl M, Arridge S, Betcke T and Holder D 2014 Stroke type differentiation using spectrally constrained multifrequency EIT: evaluation of feasibility in a realistic head model *Physiol. Meas.* **35** 1051–66
Martins T C *et al* 2019 A review of electrical impedance tomography in lung applications: theory and algorithms for absolute images *Annu. Rev. Control* **48** 442–71
Meghdadi A H, Popovic D, Rupp G, Smith S, Berka C and Verma A 2019 Transcranial impedance changes during sleep: a rheoencephalography study *IEEE J. Transl. Eng. Health Med.* **7** 1–7
Melis A 2017 Gaussian process emulators for 1D vascular models *PhD Thesis* University of Sheffield
Melis A 2018 openbf: Julia software for 1d blood flow modelling https://github.com/INSIGNEO/openBF
Melis A, Clayton R H and Marzo A 2017 Bayesian sensitivity analysis of a 1d vascular model with gaussian process emulators *Int. J. Numer. Methods Biomed. Eng.* **33** e2882
Michel C M and Brunet D 2019 EEG source imaging: a practical review of the analysis steps *Front. Neurol.* **10** 325
Min M, Kõiv H, Priidel E, Pesti K and Annus P 2019 Noninvasive acquisition of the aortic blood pressure waveform *Wearable Devices—the Big Wave of Innovation* (Rijeka: InTech)
Misaki M, Savitz J, Zotev V, Phillips R, Yuan H, Young K D, Drevets W C and Bodurka J 2014 Contrast Enhancement by combining t1- and t2-weighted structural brain MR images *Magnetic Resonance in Medicine* **74** 1609–20
Newell J C, Blue R S, Isaacson D, Saulnier G J and Ross A S 2002 Phasic three-dimensional impedance imaging of cardiac activity *Physiol. Meas.* **23** 203–9
Nielsen J D, Madsen K H, Puonti O, Siebner H R, Bauer C, Madsen C G, Saturnino G B and Thielscher A 2018 Automatic skull segmentation from MR images for realistic volume conductor models of the head: assessment of the state-of-the-art *NeuroImage* **174** 587–98
Pesti K, Kõiv H and Min M 2019 Simulation of the sensitivity distribution of four- electrode impedance sensing on radial artery *2019 IEEE Sensors Applications Symp. (SAS)* pp 1–6
Proença M, Braun F, Lemay M, Solà J, Adler A, Riedel T, Messerli F H, Thiran J-P, Rimoldi S F and Rexhaj E 2020 Non-invasive pulmonary artery pressure estimation by electrical impedance tomography in a controlled hypoxemia study in healthy subjects *Sci. Rep.* **10** 21462
Raaijmakers E, Marcus J T, Goovaerts H G, Vries P M J M, Faes T J C and Heethaar R M 1996 The influence of pulsatile flow on blood resistivity in impedance cardiography *Proc. 18th Annual Int. Conf. IEEE Engineering in Medicine and Biology Society* 5, pp 1957–8

Sakka L, Coll G and Chazal J 2011 Anatomy and physiology of cerebrospinal fluid, European annals of otorhinolaryngology *Head Neck Dis.* **128** 309–16

Schmitter S, Jagadeesan B, Grande A, Sein J, Ugurbil K and Moortele P V 2013 4d flow measurements in the superior cerebellar artery at 7 tesla: feasibility and potential for applications in patients with trigeminal neuralgia *J. Cardiovascular Magn. Reson.* **15** W21

Seki J, Satomura Y, Ooi Y and Seiyama T Y A 2006 Velocity profiles in the rat cerebral microvessels measured by optical coherence tomography *Clin. Hemorheol. Microcirc.* **34** 233–9

Shen H, Li S, Wang Y and Qin K-R 2018 Effects of the arterial radius and the center-line velocity on the conductivity and electrical impedance of pulsatile flow in the human common carotid artery *Med. Biol. Eng. Comput.* **57** 441–51

Shen H, Zhu Y and Qin K-R 2016 A theoretical computerized study for the electrical conductivity of arterial pulsatile blood flow by an elastic tube model *Med. Eng. Phys.* **38** 1439–48

Silva O L, Lima R G, Martins T C, Moura F S, Tavares R S and Tsuzuki M S G 2017 Influence of current injection pattern and electric potential measurement strategies in electrical impedance tomography *Control Eng. Pract.* **58** 276–86

Song J, Chen R, Yang L, Zhang G, Li W, Zhao Z, Xu C, Dong X and Fu F 2018 Electrical impedance changes at different phases of cerebral edema in rats with ischemic brain injury *BioMed Res. Int.* **2018** 1–10

Song J *et al* 2013 Anatomically accurate head models and their derivatives for dense array eeg source localization *Funct. Neurol. Rehabil. Ergon.* **3** 275–93

Tidswell T, Gibson A, Bayford R H and Holder D S 2001 Three-dimensional electrical impedance tomography of human brain activity *NeuroImage* **13** 283–94

Towers C M, McCann H, Wang M, Beatty P C, Pomfrett C J D and Beck M S 2000 3d simulation of EIT for monitoring impedance variations within the human head *Physiol. Meas.* **21** 119–24

Vikner T, Nyberg L, Holmgren M, Malm J, Eklund A and WÅhlin A 2019 Characterizing pulsatility in distal cerebral arteries using 4d flow MRI *J. Cerebral Blood Flow Metab.* **40** 2429–40

Visser K R 1989 Electric properties of flowing blood and impedance cardiography *Ann. Biomed. Eng.* **17** 463–73

Visser K R 1992 Electric conductivity of stationary and flowing human blood at low frequencies *Med. Biol. Eng. Comput.* **30** 636–40

Vorwerk J, Cho J-H, Rampp S, Hamer H, Knösche T R and Wolters C H 2014 A guideline for head volume conductor modeling in EEG and MEG *NeuroImage* **100** 590–607

Wagshul M E, Eide P K and Madsen J R 2011 The pulsating brain: a review of experimental and clinical studies of intracranial pulsatility *Fluids Barriers CNS* **8** 5

Costelar C, Flürenbrock F, Korn L C, Benninghaus A, Misgeld B J E, Shchukin S I, Radermacher K and Leonhardt S 2019 FEM simulation of bioimpedance-based monitoring of ventricular dilation and intracranial pulsation *Int. J. Bioelectromagn.* **21** 7–20

Zhang H J, Shen H, Li Y J and Qin K R 2020 An *in vitro* circulatory device for studying blood flow electrical impedance in human common carotid arteries *2020 IEEE 16th Int. Conf. on Control Automation (ICCA)* pp 1518–22